Dynamic surface roughness profiler

Brad Kimbrough, Neal Brock, James Millerd

4D Technology Corporation, 3280 E. Hemisphere Loop, Suite 146, Tucson, AZ 85706
(520) 294-5600, (520) 294-5601 Fax, brad.kimbrough@4dtechnology.com

A dynamic profiler is presented that is capable of precision measurement of surface roughness in the presence of significant vibration or motion. Utilizing a special CCD camera incorporating a micro-polarizer array and a proprietary LED source, quantitative measurements were obtained with exposure times of <100 μsec. The polarization-based interferometer utilizes an adjustable input polarization state to optimize fringe contrast and signal to noise for measurement of optical surfaces ranging in reflectivity from 1 to 100%. A new phase calculation algorithm is presented that nearly eliminates phase-dependent errors resulting in shot noise limited performance. In addition to its vibration immunity, the system's light weight, <5 kg, compact envelope, 24 x 24 x 8 cm, integrated alignment system, and multiple mounting options facilitate use both directly resting on large optical surfaces and directly mounted to polishing equipment, stands, gantries and robots. Measurement results presented show an RMS repeatability <0.005 nm and an RMS precision < 0.1nm which are achieved without active vibration isolation.

Keywords: Interferometer, Optical Testing, Surface Roughness, Profilometer.

1. INTRODUCTION

The microscopic surface roughness of optics is becoming increasingly critical to the performance of telescopes and precision optical equipment. For example, in proposed NASA exo-planet detection missions, the electromagnetic radiation reflected from the orbiting planet may be 10 orders of magnitude less than radiation emitted from the star. Surface roughness on the optics of the telescope is currently the limiting factor in direct imaging of exoplanets because the direct star light is scattered outside the stars primary image, obscuring the planet. X-ray telescopes have similar requirements for ultralow surface roughness, but they are further complicated by their complex shape, making inspection with conventional metrology tools impractical. Manufacturing the next generation of telescope optics requires both high quality polishing technologies for complex shapes and metrology tools capable of rapidly measuring surface quality across a very large aperture.

Currently, there are no commercially available solutions that can provide surface roughness measurements at arbitrary points on large optical surfaces in-situ without the need for vibration isolation. Current state-of-the-art experimental systems are often modified commercial instruments that are suspended over a surface. These require expensive vibration isolation equipment because they are extremely sensitive to any motion, on the order of 10's of nanometers. The other alternative is to produce small area replicas and measure them off-line. Making a replica is time consuming, may not accurately represent the actual surface, and is potentially harmful to a precision optical surface. Furthermore, the specifications for the surface finish on the next generation of telescope optics are getting increasingly tighter with wider spatial bandwidth requirements.

A significant challenge to high precision on-machine metrology is the requirement for vibration control and or significant vibration immunity. For interferometric measurements, the primary technique for obtaining vibration immunity is rapid measurement acquisition, typically sub 100 usec. One of the principal techniques for rapid phase measurement is the spatial carrier phase shifting method which utilizes a single interferogram to extract phase information.[1] In this technique, a spatial carrier, typically in the form of high frequency tilt fringes, is applied to the interferogram. The intensity profile of the modulated spatial carrier interferogram is recorded and then analyzed to determine the phase. The primary advantage of the spatial phase measurement technique over temporal phase measurement is that only one image is required, allowing acquisition times several orders of magnitude smaller than in

Optical Manufacturing and Testing IX, edited by James H. Burge, Oliver W. Fähnle, Ray Williamson,
Proc. of SPIE Vol. 8126, 81260H · © 2011 SPIE · CCC code: 0277-786X/11/$18 · doi: 10.1117/12.893557

temporal phase shifting. Rapid acquisition offers both significant vibration immunity, and the ability to measure dynamic events.

A novel approach to spatial phase measurement has been developed by 4D Technology Corporation called the *pixelated mask spatial carrier method*.[2-4] In this technique, the relative phase between the carrier and the test wavefront is modified on a pixel-by-pixel basis by a micro-polarizer phase shifting array placed just prior to detection. This technique has been successfully implemented in commercial vibration insensitive Twyman-Green and Fizeau interferometers with wavelengths from the infrared through UV.[5-9]

This paper presents a portable, high precision, vibration immune surface roughness profiler which utilizes 4D Technology's pixelated phase mask sensor. This paper is arranged in the following manner. In section 2 the theory of operation is presented and design challenges discussed. In section 3 the prototype system is presented along with several different mounting schemes. Section 4 discusses the theory and performance of a new phase calculation algorithm. Finally, in section 5 performance measurement results are presented and discussed.

2. THEORY OF OPERATION

2.1 Functional Layout

The basic layout of the dynamic surface roughness profiler is shown in figure 1. Functionally, the dynamic profiler is an epi-illuminated polarization interference microscope utilizing a Linnik interference objective and 4D Technology's pixelated polarization mask based phase sensor. This system is composed of three major sections: (1) A Kohler illuminator utilizing a high brightness 460nm LED source with adjustable output polarization. (2) A Linnik interference objective with orthogonally polarized test and reference channels, and (3) A 1.5 Mpix, low noise CCD camera with a pixelated polarization mask.

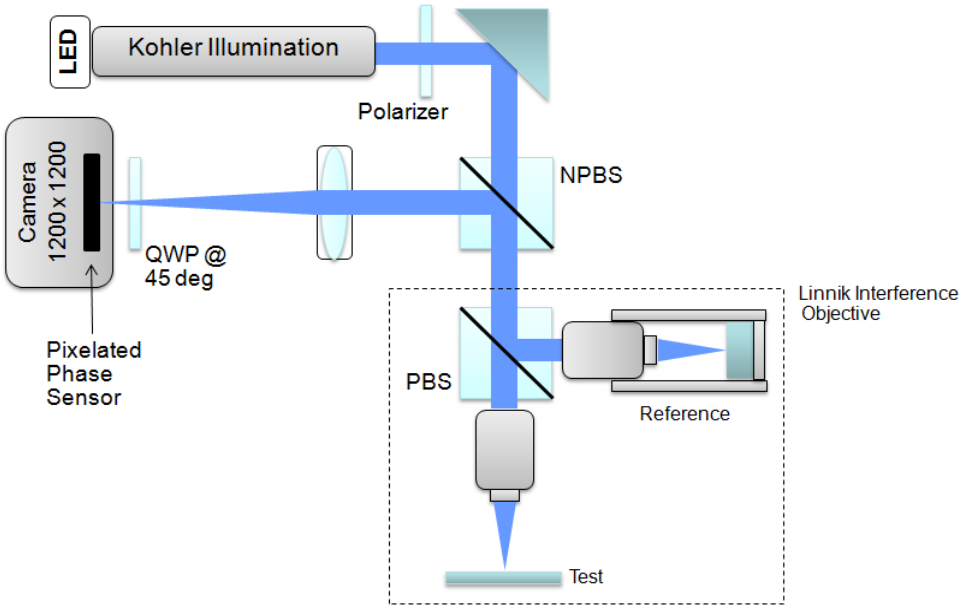

Figure 1. Functional layout of the dynamic surface roughness profiler.

2.2 Operational Description

System illumination is provided by the Kohler illuminator with an adjustable polarizer at its output. The illumination path is folded into the microscope imaging path via a non-polarizing 50/50 beam splitter. Per definition, the Kohler illuminator images the source at the entrance pupil of the Linnik objectives.

The polarization beam splitter in the Linnik objective sends the p-polarized light to the test object and the s-polarized light to the reference mirror. The reference mirror is a coated fused silica super smooth flat with a 25% reflectivity. The test to reference intensity beam ratio may be adjusted with the illumination system polarizer, allowing optimization of fringe contrast.

Upon return from the test and reference surfaces, the test and reference beams recombine at the polarizing beam splitter and exit the Linnik objective. Both beams then pass back to the non-polarizing beam splitter where half of the intensity is directed toward the camera via the system tube lens. The tube lens has an efl of 200mm and images the object and reference surfaces at the CCD camera.

Just prior to the camera both beams pass through a quarter wave plate at 45 degrees which converts the p-polarized test beam into right-hand circular polarization and the s- polarized reference beam into left hand circular polarization. Both beams then pass through the pixelated polarization mask forming an interference pattern at the detector.

2.3 Design Challenges

There are two significant challenges associated with use of the pixelated phase sensor in a microscope configuration. The first challenge is obtaining a compact source with the necessary brightness to allow short integration times. The second is polarization control necessitated by the requirement that the test and reference beams be orthogonally polarized for the pixelated polarization mask phase sensor.

2.3.1 Illumination Source

The primary factors driving source selection were integration time, size, and heat load. In order to maintain integration times below 100usecs when measuring objects with 1% reflectivity, a high brightness source was necessary. This requirement coupled with the desire for a small form factor and minimal heating led to the development of a proprietary 460nm LED source. The source is used in a Kohler illumination arrangement with a polarizer at the output and is fed into the imaging path through a non-polarizing beam splitter. Adjustment of the illumination polarization allows maximization of fringe contrast for different test object reflectivities.

2.3.2 Polarization Control

Use of the pixelated phase sensor requires that the test and reference beams of the interferometer be orthogonally polarized. Due to the narrow angular tolerance on polarization control coatings it is necessary to place the polarization beam splitter used in the interference objective in collimated or nearly collimated space. Of the three standard microscopic interference objectives, Michelson, Mirau, and Linnik, only the Linnik objective layout allows placement of the polarizing beam splitter in the pseudo-collimated space at the objective entrance pupil. Because of this placement, the Linnik objective type offers the largest working distance of all interference objectives which provides a margin of safety especially for magnifications greater than 50X. The polarization requirement coupled with the desire to have a compact design presented further challenges due to the number of optical folds in the beam path.

3. PROTOTYPE DESIGN

3.1 Measurement Head

For maximum flexibility, a compact and lightweight profiler head is a requirement. The prototype system designed weighs less than 5 kg and fits into a compact envelope of 24 x 24 x 8 cm, figure 2. The compact and lightweight design enables the head to be lifted with one hand for repositioning on a measurement surface. Its light weight also simplifies the requirements and cost for positioning systems such as gantries or robots.

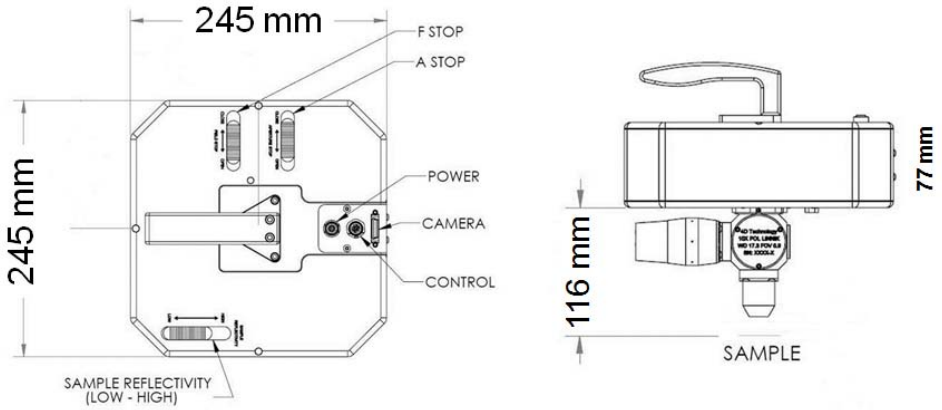

Figure 2. Schematic diagram of dynamic surface roughness profiler head.

3.2 Mounting Schemes

A versatile and flexible mounting scheme was designed to meet the very different mounting requirements for large optic manufacturers. The primary means for mounting the profiler is a tilt and focus adjustable tripod that enables the profiler to be mounted directly onto the surface of a large optic. Lens tissue can be secured to the Teflon tripod contact pads to protect the surface. Small optics can be place directly under the tripod-mounted profiler making it capable of measuring an optic of any diameter. The profiler can also be mounted directly to a polishing robot with a chuck interface located on the top of the head or to existing gantries or stands with a dove-tail interface located on backside. Figure 3 shows the engineering prototype of the dynamic surface roughness profiler mounted to a tripod base, left, and mounted to a polishing machine, right. The flexible mounting schemes facilitate use both directly resting on large optical surfaces and directly mounted to polishing equipment, stands, gantries and robots.

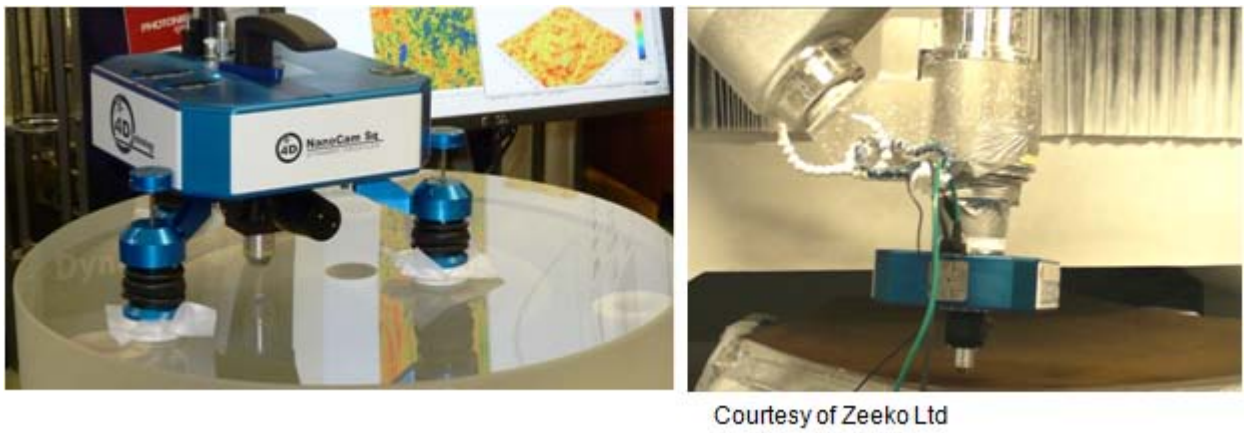

Figure 3. Dynamic surface roughness profiler mounted to tripod on left and robotic polishing tool on the right..

4. PHASE CORRECTION ALGORITHM

4.1 Foundation

High precision measurements necessitate that residual errors in the system are minimized. Phase-dependent measurement errors can be induced in both temporal and spatial phase measurements by a variety of sources such as vibration and non-linear phase-shifts. This type of measurement error presents a particular challenge because it varies in magnitude both spatially and temporally between each measurement. It typically manifests as "fringe print-through" where a small component of the intensity fringe pattern appears in the measured surface. In this section we present an algorithm that is capable of mitigating phase-dependent measurement error on-the-fly. We present results where the error has been reduced down to the shot noise limit for a dynamic system.

Regardless of the technique, all phase calculation processes ultimately return a phase value which is computed as the arctangent of the ratio of two values. These two values will be referred to as the numerator, **N**, and the denominator, **D**, terms. Each of these terms is a function of the actual phase value, **θ**, being measured, and is generally calculated from a set of measured interferograms. The simple relationship between the calculated phase, **θ`**, and **N** and **D** is shown in equation 1.

$$Tan(\theta') = \frac{N(\theta)}{D(\theta)} \tag{1}$$

A general expression for **N** and **D** is given in equations 2 and 3.

$$N(\theta) = y_o + a_y Sin(\theta + \phi_y) \tag{2}$$

$$D(\theta) = x_o + a_x Cos(\theta + \phi_x) \tag{3}$$

Together, equations 2 and 3 are the parametric equations for a general ellipse where each {x, y} point on the ellipse is given by {D(θ), N(θ)}. The phase calculation process is error free if the following condition holds for all values of calculated phase:

$$\theta' = \theta + \theta_o \tag{4}$$

where $\boldsymbol{\theta_o}$ is a constant. In order for equation 1.4 to be true, the following conditions must be met:

$$x_o = 0 \quad and \quad y_o = 0 \tag{5}$$

$$a_x = a_y \tag{6}$$

$$\phi_x = \phi_y \tag{7}$$

Simply put, the **N** and **D** terms must not have any offset, the amplitudes must be equal and the phase must be in quadrature. Associating the {**D**, **N**} values with {x, y} coordinate pairs, the conditions for error free phase calculation are seen to be the requirements that all {**D**, **N**} coordinate pairs fall on a circle centered at the origin, with amplitude $r=a_x=a_y$. In general, however, due to unavoidable errors in the phase calculation process, all {**D**, **N**} coordinate pairs will fall on an ellipse centered at $\{x_o, y_o\}$. The error in the phase calculation is equal to the difference between the parameterizing angle, **θ**, and the coordinate angle, **θ`**. The relationship between the parameterizing angle and the coordinate angle for a general ellipse is shown in figure 4.

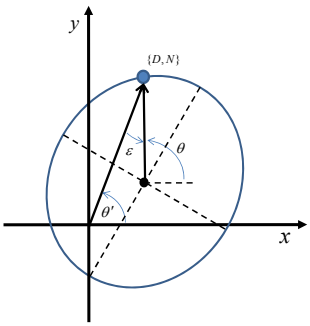

Figure 4: General ellipse plot showing the parametric angle, θ, the coordinate angle, θ`, and the difference angle, ε=θ`-θ, for a given point {D, N}.

The parameter angle is always equal to the coordinate angle in a circle centered at the origin; this is not the case for a non-centered circle or an ellipse, resulting in the well known single and double frequency print through errors. Lissajous curves are created by plotting the {**D**, **N**} coordinate pairs as defined in equations 1.2 and 1.3. Three different curves were created corresponding to an offset error, and amplitude error, and a phase error. These curves are shown in figure 5a. For each of the curves given in figure 1, the difference between the parametric angle, θ, and the coordinate angle, θ`, at each point is plotted in figure 5b. Generally, offset, amplitude and phase errors occur simultaneously, and the phase calculation error will be a non-linear combination of these three error sources.

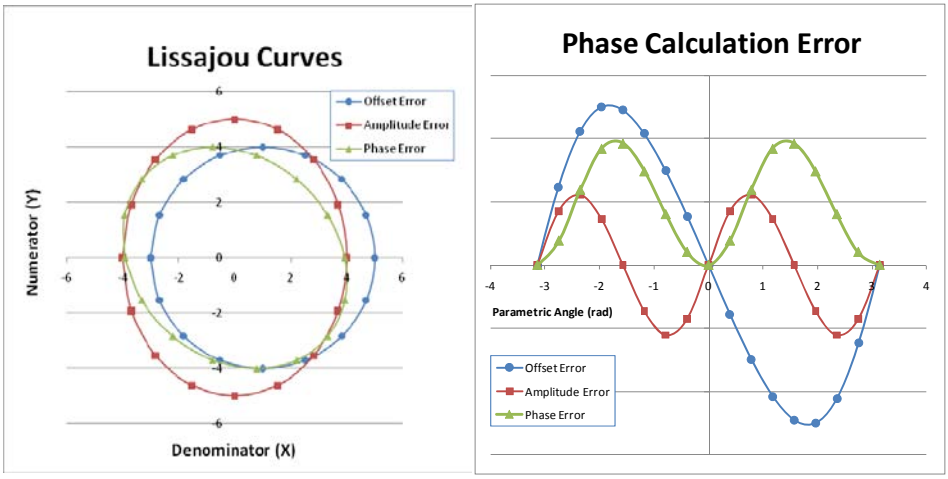

Figure 5. A. Lissajous plots associated with offset, amplitude, and phase errors where coordinate points given by parametric equations 1.2 and 1.3. B. Phase calculation error given by the difference between the coordinate and parametric angle of each point in the curves of figure 2a.

The use of Lissajous curves in the analysis of phase shifting interferometry has been discussed by Kinnstaetter et al.[10], who utilizes Lissajous figures in the analysis of systematic errors; intensity variation, reference phase errors, vibrations, and nonlinearities of the photo detector. They also present a self calibrating technique for correction of phase step calibration errors. Farrell and Player[11] utilize ellipse fitting and Lissajous figures to calculate the phase difference between interferograms. The intensity bias and modulation of the interferograms is also calculated. Their technique utilizes the whole fringe field to detect and quantify phase and intensity changes between frames. At least one fringe across the field is desirable, and this method performs best when the fringe fields are formed with uniform illumination. The idea of using the calculated bias, offset, and phase shift to correct the measured fringe fields which are then used in standard phase shifting calculations is also presented in their paper.

4.2 Ellipse Fitting and Measurement Transformation

Ignoring a constant phase offset and setting $\varphi = (\varphi_y - \varphi_x)$, equations 2 and 3 may be written as:

$$N(\theta) = y_o + a_y Sin(\theta + \phi) \tag{8}$$

$$D(\theta) = x_o + a_x Cos(\theta) \tag{9}$$

Equations 8 and 9 describe a general ellipse with offset $\{x_o, y_0\}$, and semi-major and minor amplitudes of $\{a_x, a_y\}$. The ellipse orientation angle, α, referenced to the x-axis is given by:

$$Tan(2\alpha) = \frac{2a_x a_y Sin(\phi)}{a_x^2 - a_y^2} \tag{10}$$

The parametric coefficients, $\mathbf{\{x_o, y_o, a_x, a_y, \alpha\}}$ may be determined through fitting the Lissajou curves shown in figure 2 to a general ellipse. Using the best fit ellipse parameters, the measurement numerator and denominator points are transformed to lie on a circle centered at the origin. In other words, the measured parameters are used to remove the offsets, equalize amplitudes and orthogonalize the **N** and **D** terms. This transformation is shown in equation 14.

$$\{D_t, N_t\} = R(-\alpha) \cdot \{1, \tfrac{a_x}{a_y}\} \cdot R(\alpha) \cdot \{D - x_o, N - y_o\} \tag{11}$$

where R is the rotation matrix.

4.3 Measurement Process

Let's say we have an interferometer that on each measurement returns two interferograms, one phase shifted approximately 90 degrees with respect to the other. The first interferogram in this pair will be designated **D**(θ), the second **N**(θ). Using this interferometer we take a series of six measurements $\{\mathbf{m_1}.....\mathbf{m_6}\}$, where a phase offset $\{\boldsymbol{\delta_2}.....\boldsymbol{\delta_6}\}$ is introduced between each measurement, figure 6A. Choosing one field point (pixel) in the interferogram, all the $\{\mathbf{D}_i, \mathbf{N}_i\}$ points are plotted as shown in figure 6B.

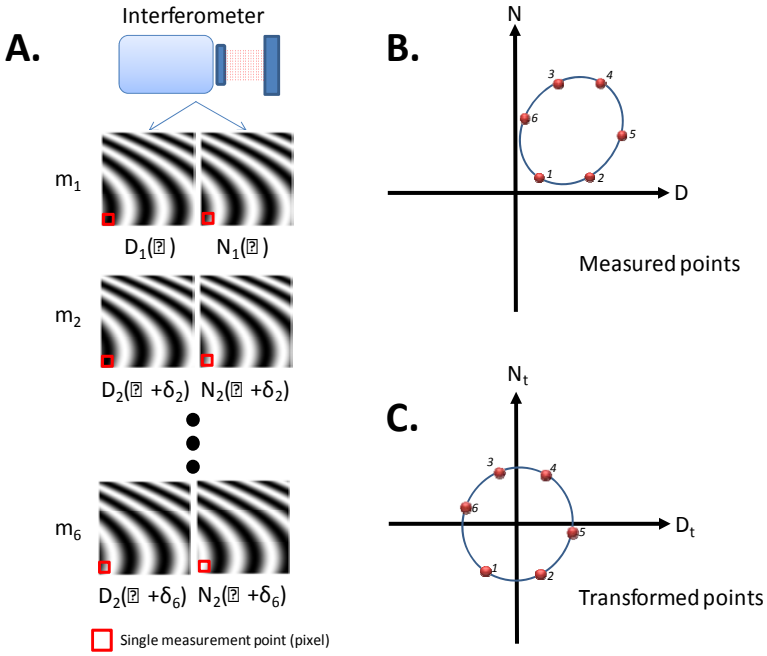

Figure 6: Phase measurement process. A. On each measurement an interferometer returns two interferograms, each phase shifted approximately 90 degrees with respect to the other. A series of six measurements are made where a phase offset is introduced between the measurements. B. For a single pixel, highlighted red box, all {D, N} pairs are plotted forming an offset ellipse as shown. From these points a best fit ellipse is determined. C. Using the ellipse fit coefficients, all {D, N} pairs are transformed to lie on a circle centered at the origin. The phase at each point is given by the arctangent of the ratio of the N_t to D_t terms. Steps B. and C. are repeated for all points in the field.

The next step in the measurement process is to find the best fit ellipse to the measured points in order to determine the parametric coefficients, $\{\mathbf{x_o}, \mathbf{y_o}, \mathbf{a_x}, \mathbf{a_y}, \boldsymbol{\alpha}\}$, as given by equations 8-10. Using these coefficients, the **N** and **D** terms are transformed to satisfy conditions given in equations 5-7 for an error free phase measurement by using the transformation given in equation 14, figure 6C. Finally, the phase is determined by taking the arctangent of the ratio of the N_t and $\mathbf{D_t}$ terms. This process is repeated for all points in the field.

4.4 Measurement Results

One advantage of using the pixelated polarization mask phase sensor is that the mechanisms leading to phase-dependent measurement error are static for a given test setup, and thus it is possible to correct for them. The dominate mechanism is polarization mixing between the test and reference beams which is caused by birefringence in both the common and non-common path portions of the interferometer. For a given test setup the polarization mixing is static, although it may not be spatially uniform, thus by using the procedure of 4.3 it is possible to measure the error on a pixel by pixel basis.

In terms of the discussion of section 4.1, polarization mixing primarily results in offset terms in the numerator and denominator of equations 1 and 2 giving single frequency print-through in the phase measurement. There is also a change in the amplitude balance which results in a lower amplitude double frequency print-through error. Figure 7 shows the results of a single phase measurement on a super smooth flat (surface roughness <0.1nm). Tilt fringes were intentionally introduced so that the phase-dependent error is evident as a sinusoidal variation across the horizontal direction. As can be seen, the standard measurement procedure results in about 15nm of single frequency print through (or approximately λ/50). If a flat field calibration procedure is used, which is roughly equivalent to normalizing the offset coefficients, the single frequency print-through is mostly eliminated, but a double frequency component with 3nm peak-to-valley remains. Application of the full phase correction process outlined in section 4.3 above results in near elimination of both single and double frequency print-through giving a 0.3 nm (λ/2000) peak-to valley error which is below the shot noise limit. Note that these are single shot, not averaged measurements.

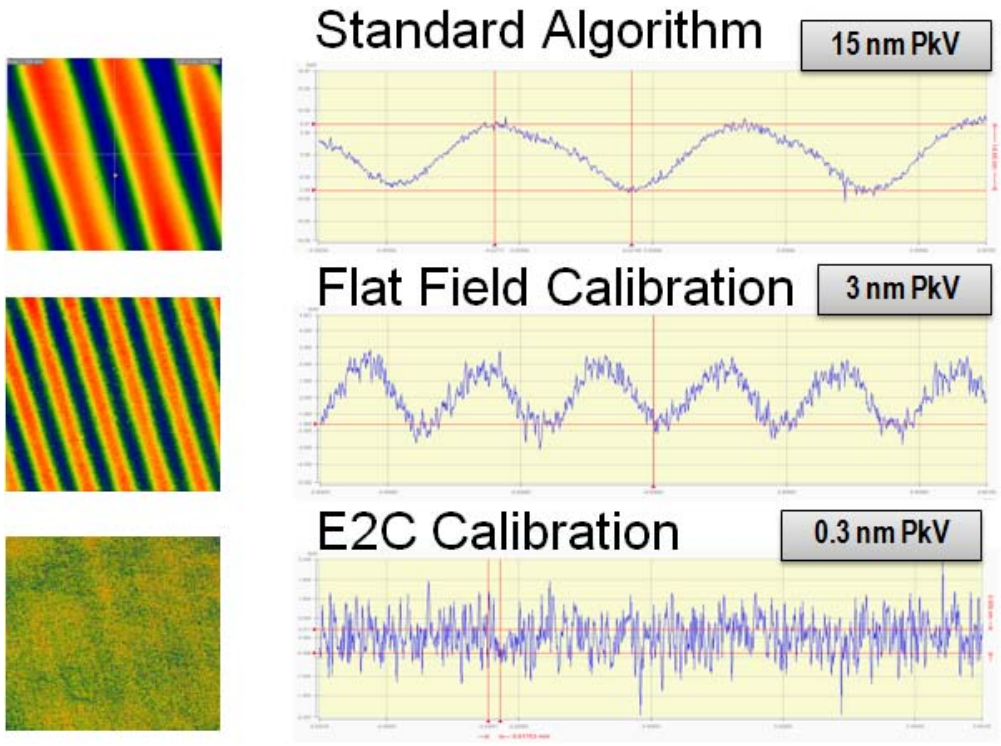

Figure 7: Comparison of phase measurement calibration procedures.

5. MEASUREMENT PERFORMANCE

General measurement performance specifications for the dynamic surface profiler are listed in Table 1. These specifications were determined through measurements of a super smooth surface on a non-vibration isolated table.

Table 1. Dynamic surface profiler general measurement specifications.

	RMS (nm)	PVq (nm)
Shot Noise	**0.55**	----------
Uncalibrated Accuracy		
Low Order (shape)	**0.98**	**3.0**
High Order (roughness)	**0.1**	**0.4**
16 Averages		
Precision	**0.08**	**0.3**
Repeatability	**0.004**	**0.01**

One of the advantages of the dynamic surface roughness profiler over temporal or vertical scanning systems is the ability to ability to average a very large number of measurements. One technique for determining measurement noise is by taking difference measurements. This is simply two measurements, or two averaged measurements taken at the same test point and then subtracted. As long as the system is stable, the difference measurement should be uniformly distributed shot noise with an RMS value equal to $\sqrt{2}$ times the single measurement value. Figure 8 shows the measured vs. theoretical shot noise values for 16 through 2000 average difference measurements taken on a super smooth flat with a 10X objective. The measurements were taken on a non vibration isolated table. These measurements demonstrate the ability of the dynamic surface profiler to obtain very large average measurements with shot noise limited performance over time scales exceeding 1 minute.

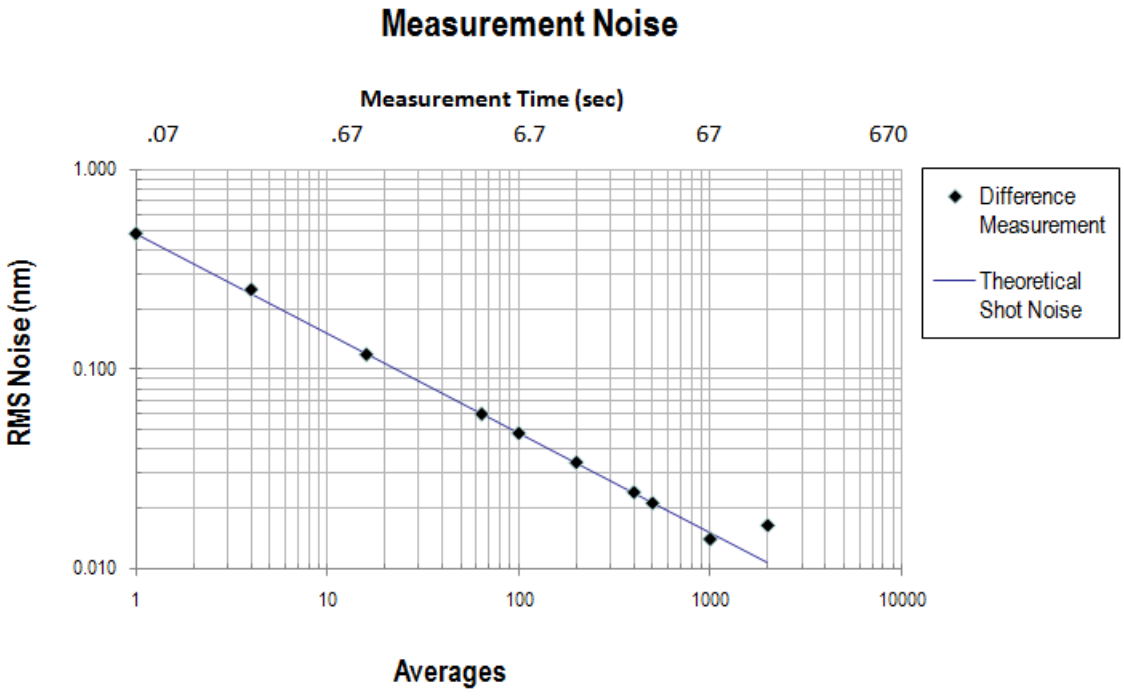

Figure 8: Measurement noise of the dynamic surface profiler demonstrating shot noise limit performance out through 1000 averages.

The effect of averaging on RMS precision and repeatability were measured on a super smooth flat with the 10X objective. The results of these measurements are shown in figure 9. Both precision and repeatability trend as expected with an increasing number of averages. It is not until >1000 averages that the trend in performance benefit with averaging starts to decrease.

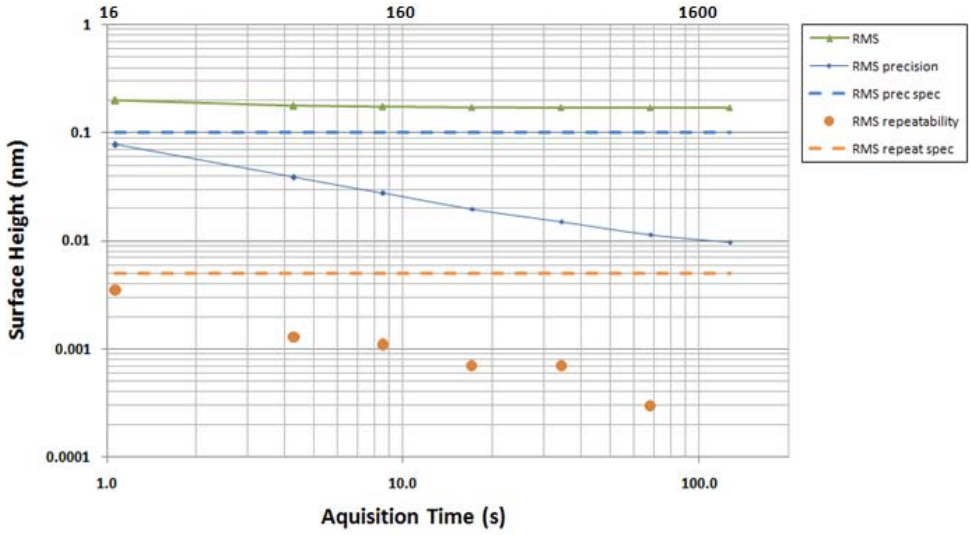

Figure 9: Dynamic surface profiler RMS precision and repeatability measurements as a function of measurement averages.

The instrument transfer function (ITF) of the dynamic surface profiler was determined through measurements of a 40nm VLSI step. ITF curves for the 5X, 10X, and 20X objectives are shown as solid curves in figure 10. The dashed curves give the theoretical ITF performance. All measurements demonstrate close agreement with theory. The secondary hump in the 5X ITF curve indicates under-sampling at the detector.

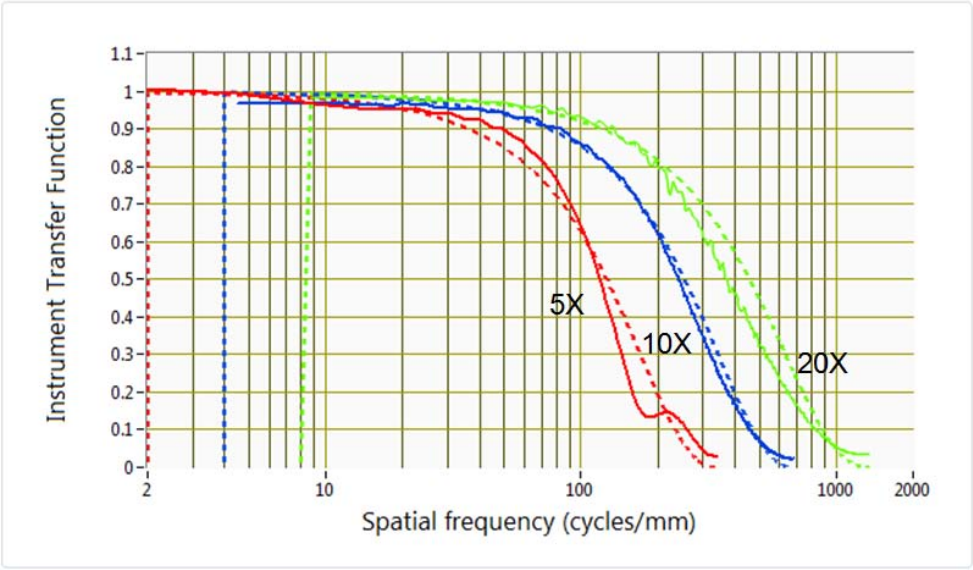

Figure 10: Dynamic surface profiler instrument transfer function (ITF) for the 5X, 10X and 20X objectives. Dashed curves give theoretical ITF performance.

6. SUMMARY

We have developed a dynamic surface profiler using a polarization based interference objective and pixelated micro-polarizer camera that is capable of measuring surface roughness in the presence of significant vibration. To achieve shot noise limited performance, we developed a correction algorithm that eliminates phase-dependent measurement error. We demonstrated the ability to measure with sub-angstrom repeatability and precision through modest averaging. Measurements with 5x, 10x, and 20x objectives show Nyquist limited performance. The portability, high measurement quality, and short acquisition time of the prototype system allow its use in a wide variety of applications ranging from surface roughness in large optics manufacturing to capture of dynamic events in MEMS actuators.

REFERENCES

1. D. Malacara, M. Servin, and Z. Malacara, “Interferogram analysis for optical testing,” (Marcel Dekker, New York, 1998).
2. J. E. Millerd, N. J. Brock, J. B. Hayes, M. B. North-Morris, M. Novak, and J. C. Wyant, "Pixelated phase-mask dynamic interferometer," Proc. SPIE 5531, 304-314, (2004).
3. North-Morris, M., Millerd, J., Brock, N., Hayes, J., and Saif, B., “Dynamic Phase-Shifting Electronic Speckle Pattern Interferometer.” Proc. SPIE 5869:50, (2005)
4. J. E. Millerd in “Fringe 2005,” edited by W. Osten, (Springer, New York, 2005), pg 640.
5. B. Kimbrough, J. Millerd, J. Wyant, J. Hayes, “Low Coherence Vibration Insensitive Fizeau Interferometer,” Proc. SPIE 6292, (2006).
6. Kimbrough, B., Frey, E., Millerd, J., “Instantaneous phase-shift Fizeau interferometer utilizing a synchronous frequency shift mechanism.” Proc. SPIE 7063, (2008)
7. B. T. Kimbrough, “Dynamic Fizeau Interferometers,” in “Fringe 2009,” edited by W. Osten, M. Kajawinska, Springer, New York, 445, (2009).
8. M. North Morris, "Dynamic Interferometry for on-Machine Metrology," in Frontiers in Optics, OSA Technical Digest (CD), paper STuA3.
9. M. North Morris, M. Naradikian, J. Millerd, “Noise reduction in dynamic interferometry measurements,” Proceedings of the SPIE, 7790, (2010).
10. K. Kinnstaetter, Adolf W. Lohmann, Johannes Schwider, and Norbert Streibl, "Accuracy of phase shifting interferometry," Appl. Opt. 27, 5082-5089 (1988)
11. C T Farrell and M A Player, “Phase step measurement and variable step algorithms in phase-shifting interferometry,” Meas. Sci. Technol. 3 953 (1992)